ADVANCED MATERIALS INTERFACES
Open Access
www.advmatinterfaces.de

Nitrogen-Doped Amorphous Carbon Film for Enhanced Cu^{2+} Electrochemical Sensing in Marine Environments

Xueqing Zhao, Silong Zhang, Shuyuan Wang, Peng Guo, Zhenyu Wang, Guanshui Ma, and Aiying Wang**

Amorphous carbon (a-C) is a promising material for electrochemical sensing due to its wide potential window and chemical stability. However, its high resistance and limited surface activity hinder performance. Nitrogen (N) doping can improve conductivity while maintaining a low background current, but precise control of N content remains challenging. In this study, N-doped a-C films are fabricated using a high-ionization anode-layer ion source by adjusting the C_2H_2/N_2 gas ratio. The influence of N concentration on Cu^{2+} detection performance is systematically evaluated. Moderate N doping (≈12.9 at.%) facilitates the formation of sp^2-hybridized carbon and nitrogen-containing functional groups, significantly enhancing electrochemical activity. The optimized electrode exhibits a wide linear detection range from 8×10^{-3} to 5 mM and a low detection limit of 8×10^{-3} mM in 3.5 wt% NaCl solution, sufficient for monitoring copper alloy crevice corrosion (≈0.1 mM). The electrodes also show excellent repeatability, reproducibility, and long-term stability. Theoretical calculations indicate that increased sp^2 content and C—N bonds enhance Cu^{2+} adsorption and electron transfer, thereby improving sensor performance via N doping.

1. Introduction

Corrosion remains a persistent challenge in marine economic development. The presence of highly concentrated electrolytes significantly accelerates the degradation of metals and alloys, increasing the risk of catastrophic accidents in marine engineering systems.[1] Copper-based alloys are widely used in marine engineering because of their excellent corrosion resistance and favorable physical properties.[2–4] Research has shown that during the crevice corrosion of these alloys, the dissolution of the copper (Cu) element at the anode interface occurs earlier than the dissolution of nickel (Ni) and iron (Fe) elements. Therefore, monitoring of copper ions (Cu^{2+}) level indicates the propensity of initiation of corrosion locations and services lifetime prediction for marine metallic components.[5,6]

Various electrode materials for copper ion electrochemical sensor construction were explored in recent years.[7–11] Among them, Boron doped diamond (BDD) electrode has been successfully applied in metal detection due to its mechanical stability, corrosion resistance, stable surface properties, wide potential window, and excellent electrochemical activity.[12–16] Furthermore, it has been observed that the sp^3/sp^2 ratio of the BDD film significantly influences its sensing performance, with a higher level of sp^2 hybrid carbon linked to faster electron transfer, higher background current, and improved corrosion sensitivity.[17–19] However, the conditions for BDD preparation, high temperature at 800 °C or above, were much critical, which limited the application of BDD electrodes in microfabrication of microelectrode arrays and temperature-sensitive substrates.[20–23] Different from BDD electrodes, amorphous carbon (a-C) film, primarily composed of sp^2-C and sp^3-C atomic bonds, can be easily fabricated over large areas at ambient temperature using various physical vapor deposition techniques. These films also exhibit superior mechanical robustness, chemical inertness, corrosion resistance, and excellent electrochemical properties as BDD, providing a potential alternative electrochemical detection strategy in the marine environment.[24–30]

However, the high resistance and low surface activity of a-C films currently limit their rapid response and high sensitivity as electrochemical sensors. Doping elements like B, N, and P could improve the conductivity of a-C films and maintain a wide potential window as well as low background current at the same time.[31–36] Notably, unlike phosphorus and boron doping, which primarily involve red phosphorus, phosphorane, and toxic borane compounds, nitrogen doping using N_2 gas offers several

---

X. Zhao
State Key Laboratory of Green Chemical Synthesis and Conversion
College of Chemical Engineering
Zhejiang University of Technology
Hangzhou 310032, P. R. China

X. Zhao, S. Zhang, P. Guo, Z. Wang, G. Ma, A. Wang
State Key Laboratory of Advanced Marine Materials
Zhejiang Key Laboratory of Extreme-environmental Material Surfaces and Interfaces
Ningbo Institute of Materials Technology and Engineering
Chinese Academy of Sciences
Ningbo 315201, P. R. China
E-mail: maguanshui@nimte.ac.cn; aywang@nimte.ac.cn

S. Wang
Jiangxi Copper Company Limited
Nanchang 330095, P. R. China

The ORCID identification number(s) for the author(s) of this article can be found under https://doi.org/10.1002/admi.202500583

DOI: 10.1002/admi.202500583

advantages, including easy fabrication over large areas at room temperature, non-toxic processing, and low cost.[37–39] Nilkar et al. deposited N-DLC by dielectric barrier discharge plasma technique with CH_4 and N_2 gas.[40] The doping of N atoms was found to act as effective donors, enhancing the electronic transmission by graphitization bonding structure, raising the Fermi level, and narrowing the band gap. The wide potential window, low parasitic current, and nearly reversibility by N doping in an a-C film were also reported.[35]

In this work, we fabricated a series of N-doped a-C films by a homemade anode-layer ion source (ALIS) technique. The concentration of doped nitrogen was varied by adjusting the ratio between introduced C_2H_2 and N_2 sources. The dependence of nitrogen concentration on the atomic bonding structure, surface property, and electrochemical properties of a-C films was analyzed. The performance of copper ions (Cu^{2+}) detection was investigated on N-doped a-C film in 3.5 wt% % NaCl solution (average salinity of sea water) by differential pulse voltammetry (DPV) method. The electrode repeatability, reproducibility, and stability were evaluated in terms of microstructural evolution and electrochemical properties. In addition, density functional theory (DFT) calculations were employed to clarify the mechanism of the improvement of Cu^{2+} detection performance. All results demonstrated that N-doped a-C films are promising materials for corrosion monitoring of copper-based marine engineering structures.

2. Result and Discussion

2.1. Components Characterization of Films

N-doped a-C was prepared by ALIS technology. By adjusting the ratio of N_2 and C_2H_2 gas flow during film deposition, the N-doped content in the film can be controlled. **Figure 1a** illustrates the schematic diagram of the deposition system. The complete XPS spectrum, as illustrated in Figure S1 (Supporting Information), displayed the pure a-C film, which was predominantly constituted of C 1s and O 1s peaks. With the increase of N_2 gas flow rate, a new peak belonging to N 1s appeared at 299.1 eV, and the N 1s peak became stronger while the C 1s peak became weaker. The fitted element composition of each sample was shown in Figure S2 (Supporting Information). Increasing the N_2 gas flow rate from 0 to 85 sccm led to the increase of nitrogen concentration in a-C films from 0 to 13.1 at.%. Thus, all the specimens were labeled as a-C, N-2.1 at.%, N-4.0 at.%, N-6.9 at.%, N-12.9 at.%, N-13.1 at.%, according to their nitrogen concentration, respectively. Noted that the doped N element almost reached saturation when the N_2 gas flow rate reached 80 sccm. In addition, after etching by Ar^+ ions, the O 1s peak almost disappeared in the XPS spectrum. The emergence of O concentration ≈6.8-8.1 at.% was mainly due to less residual oxygen in the vacuum chamber and oxygen adsorbed in air.

To further analyze the structure evolution of elements, high-resolution C 1s and N 1s XPS core level spectra were investigated. Figure 1b exhibited the C 1s core level spectra, where the peak was fitted by Gaussian (30%)-Lorentz (70%) function and decomposed into five peaks at 284.5, 285.3, 285.9, 286.3, and 288.8 eV corresponding to sp^2—C, sp^3—C, C—N, C—O, and C═O, respectively.[41] The structure evolution of C bonds influenced by nitrogen concentration was summarized in Figure 1c. As the nitrogen concentration increased from 0 at.% to 13.1 at.%, the sp^2—C bond concentration initially rose from 55.0 at.% to 57.7 at.%, then decreased to 53.13 at.%. In contrast, the sp^3—C concentration first dropped from 31.4 at.% to 7.9 at.% and then increased to 13.9 at.%. The maximum sp^2—C/sp^3—C ratio occurred at the N-12.9 at.% sample, suggesting that an optimal amount of N doping promotes the sp^2—C fraction in the film. Meanwhile, the enhanced C—N peak intensity indicated the formation of stable C—N bonds at sp^3-hybridized carbon sites, induced by nitrogen doping. More importantly, nitrogen doping enhances the electronegativity of carbon materials by forming C—N bonds, which induce localized positive charges on adjacent carbon atoms. This electronic redistribution strengthens the interaction with electrons, thereby facilitating catalytic redox reactions.[42]

The nitrogen species in nitrogen-doped carbon materials are mainly divided into four types: graphite nitrogen, pyridine nitrogen, pyrrole nitrogen, and pyridine nitrogen oxides. Figure 1d,e illustrates the N 1s core level spectra and the fitted N bond states in a-C films. Three sub-peaks were obtained by Gaussian-Lorentz decomposition in Figure 1d: the peak at 398.6 eV was assigned to pyridine N, the peak at 400.4 eV was attributed to pyrrole N, and the peak at 402.2 eV was related to graphite N.[43,44] As demonstrated in Figure 1e, both pyridinic N and pyrrolic N exhibited an increase in their concentration as the nitrogen doping content increased. Consequently, the pyridinic N increased from 1.8 at.% to 6.8 at.%, and the pyrrolic N increased from 0.2 at.% to 5.8 at.%. Due to their unhybridized lone pair electrons and strong electron-donating ability, pyridinic nitrogen species can effectively serve as Lewis base sites. As a result, nitrogen-doped carbon catalysts enriched with pyridinic nitrogen exhibit enhanced catalytic performance in redox reactions.[45,46]

Raman spectroscopy was employed as an important tool for component characterization in amorphous carbon films owing to its sensitivity to carbon bond structure and non-destructive properties. The Raman spectra of all samples were dominated by one typical broad peak from 1000 to 1800 cm^{-1}, characteristic of the amorphous nature of these films (Figure 1f). The broad peak was fitted by a Gaussian function and decomposed into two sub-peaks: the D peak centered at 1360 cm^{-1} and the G peak centered at 1580 cm^{-1}. The D peak was attributed to defects within the graphitic structure, while the G peak corresponded to the stretching vibration of two adjacent carbon atoms, which appeared at all sp^2 sites in the film. With increased nitrogen doping, the D peak intensity gradually increased, indicating a higher defect density caused by lattice distortion, sp^2 network disruption, and charge redistribution.[47] The carbon bond structure can be further elucidated by analyzing the full width at half maximum (FWHM) of the G peak, its position, and the integrated area ratio of the D and G bands (I_D/I_G) (Figure S3, Supporting Information). The FWHM of G peak was a measure of structural disorder caused by the distortion of bond length and bond angle, and the increased FWHM reflected an increase in structural disorder. The upward shift of the G peak position was attributed to the development of sp^2 content.[48] The I_D/I_G value was related to the number of sp^2 clusters and the size of sp^2 cluster grains. According to Ferrari's model, I_D/I_G value was proportional to graphite grain size (L_a) at the second stage.[49]

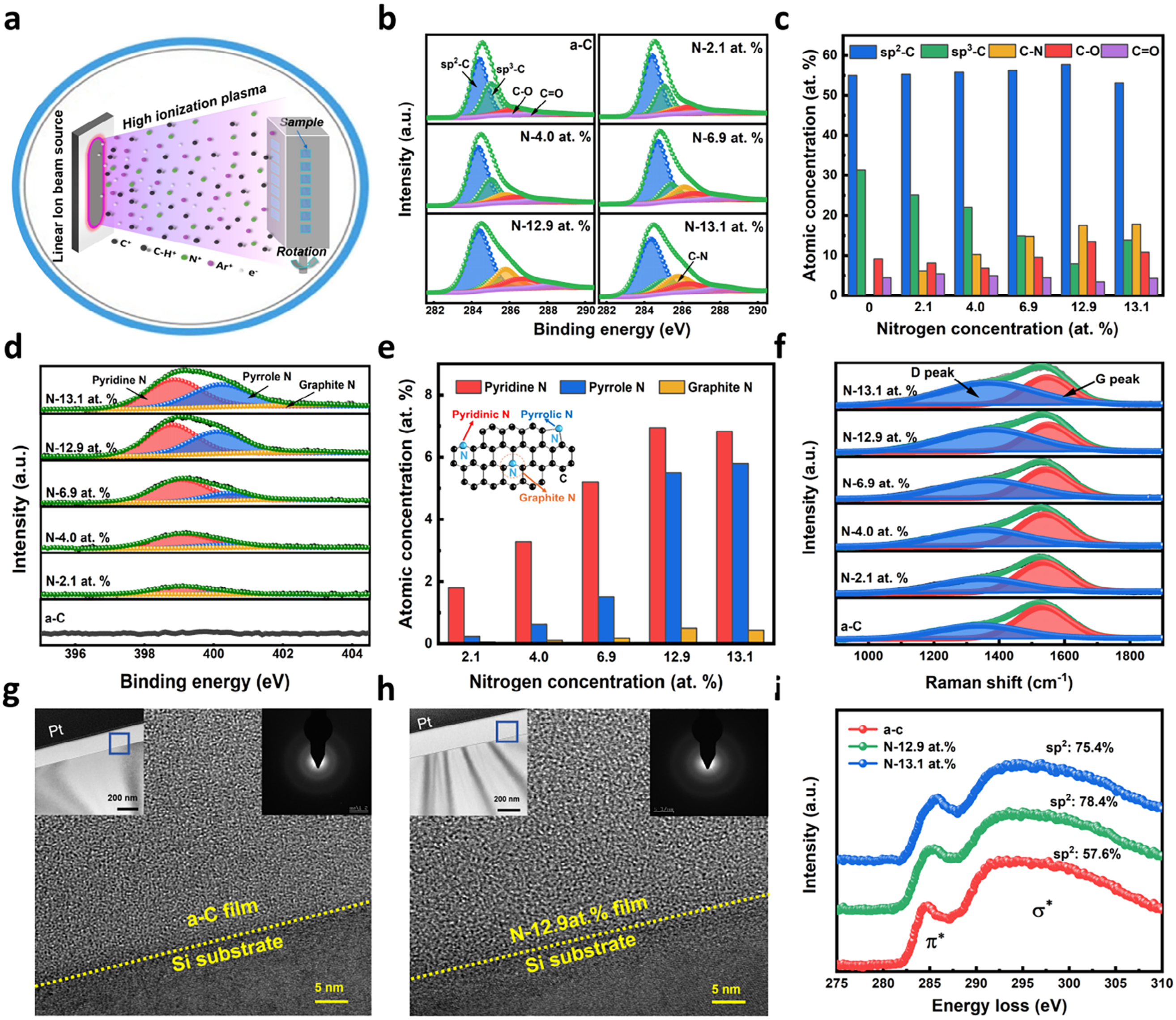

Figure 1. a) Preparation schematic of N-doped a-C films; b) Deconvolved C 1s core level XPS spectrum of a-C and N doped a-C, c) and their element concentration evolution of various carbon bonds; d) Deconvolved N 1s core level XPS spectrum of a-C and N doped a-C, e) and their concentration evolution of different nitrogen bonds; f) Raman spectra with corresponding peak decomposition; HRTEM images of a-C g), N-12.9 at.% h) and insert were the corresponding TEM images and SAED pattern; i) EELS spectra of three typical films and the calculated sp^2-C friction.

In other words, with the increase of nitrogen concentration, the G peak FWHM first decreased from 179.2 to 166.5 and then increased to 168.4, when the nitrogen concentration reached 12.9 at.%. The G peak position was shifted upward and then went downward since N-12.9 at.% sample, and the I_D/I_G increased from 0.699 (a-C) to 1.674 (N-12.9 at.%) but then decreased to 1.668 (N-13.1 at.%). These results suggest that a moderate level of nitrogen doping reduces structural disorder, enhances the formation of sp^2 sites, and promotes the growth of larger sp^2 graphite grains.[50,51] This phenomenon is consistent with previous reports. For instance, Zhou et al. found that nitrogen incorporation did not alter the amorphous structure of the film but increased the content of sp^2-clustered phases, thereby enhancing the degree of graphitization.[52] But when the nitrogen concentration reached 13.1 at.%, the nitrogen would play an opposite role. This observation is consistent with the findings of Liang et al., who reported a highway-mediated nanoarchitecture consisting of pseudo-graphitic nanodomains embedded in highly nitrogen-doped disordered segments.[53] Additionally, Raman results showed good agreement with XPS results. Nitrogen atoms were incorporated into stable covalent bonds with carbon, and moderate N doping promoted the formation of sp^2 sites. This could be due to nitrogen replacing sp^3 C—C bonds in the aromatic rings, leading to a reduction in the average coordination number and a decrease in the sp^3 hybrid composition.[54]

The TEM cross-sectional images of two typical films, a-C and N-12.9 at.% sample, were shown in Figure 1g,h. The Si substrate was totally covered by a-C and N-doped a-C film, with relatively uniform thickness between 208 and 271 nm. Then, the corresponding crystal structure of a-C and N-12.9 at.% film was analyzed through HRTEM images and SAED (upper right illustration). The a-C film without nitrogen doping exhibited dense and amorphous nanostructure, confirmed by the corresponding SAED pattern, which featured typical broad rings of amorphous structure. With nitrogen concentrations of 12.9 at.%, the films maintained their amorphous nanostructure, indicating that the incorporation of nitrogen did not change the amorphous properties of the films. Figure 1i shows the EELS spectra of three films after extracting the background with the highly oriented pyrolytic graphite as a reference. The carbon K-edge spectra, ranging from 275 to 310 eV, include the π^* peak located at 285 eV fitted by a Gaussian function and the σ^* peak with the energy window from 290 to 305 eV. The sp^2-C fraction (x) was then analyzed by the follow equation:[55,56]

$$\frac{\left(\frac{\pi*}{\sigma*}\right) film}{\left(\frac{\pi*}{\sigma*}\right) HOPG} = \frac{3 - x}{4x} \tag{1}$$

Based on the above calculation, the sp^2-C fraction of a-C film was 57.6%. The sp^2-C fraction first increased to 78.4% and then decreased to 75.4%, as the nitrogen concentration reached 12.9 at.% and 13.1 at.%, respectively. The EELS spectra further confirmed the Raman and XPS results that the sp^2-C fraction could be increased by moderate N doping, but it decreased instead when the nitrogen concentration exceeded 12.9 at.%. It has been reported that the changes in the electrochemical properties of membrane electrodes are closely related to their microstructure.[57] Specifically, electron transport in a-C films is primarily governed by sp^2-bonded carbon atoms, which is further determined by the quantity and size of sp^2 clusters within the carbon network. The increase of sp^2 clusters contributes to the formation of electron transport channels and promotes electron transport, which contributes to the rapid electrochemical response of nitrogen-doped a-C film electrodes.[58]

To investigate the effect of N doping level on surface morphology, a-C film and N-doped a-C film were observed by AFM. Figure S4a–c (Supporting Information) exhibited the 3D views of AFM image of a-C, N-4.0 at.%, N-13.1 at.% film. The surface of a-C film was relatively rough, with a root-mean-square (RMS) roughness of 0.44 nm. However, the surface morphology of N-4.0 at.% and N-13.1 at.% became smoother with the RMS roughness value down to 0.36 and 0.25 nm, respectively. It could be surmised from Figure S5d that the addition of N element resulted in a smoother film surface. Furthermore, the water contact angle also reflected the surface characteristics of the film to a certain extent. As shown in Figure S4d (Supporting Information), the contact angle of the film initially decreased from 81.7° to 69.7° and then slightly increased to 73.4°, which could be interpreted as the combined effect of sp^2-C fraction, C—N active bonds, and surface morphology.[59] On the one hand, as nitrogen doping increased, the higher sp^2-C content reduced the surface energy, while the formation of more active C—N bonds significantly increased the surface energy. As a result, the surface energy of the film increased, which made the film surface more hydrophilic and reduced the contact angle. On the other hand, the smoother surface resulted in a more hydrophobic film surface and higher contact angle according to the Wenzel model.[60] Under the joint action of those factors, when the N concentration reached 12.9 at.%, the minimum value of contact angle of 69.7° was obtained.

2.2. Electrochemical Properties

The electrochemical behaviors of a-C and N-doped a-C film were investigated. The potential windows, electrochemical activity in the Fe(CN)$_6{}^{3-/4-}$ redox system, and the electrochemical behavior in Cu^{2+} solution were studied via cyclic voltammetry (CV) method and (electrochemical impedance spectroscopy (EIS) Nyquist plots. First, the potential window (ΔE) of the electrodes was examined, as it is considered one of the most important parameters of electrode properties. It refers to the distinction between the hydrogen evolution and oxygen evolution potential of the electrode reaction, with the range where redox current density <0.2 being usually adopted as ΔE. In addition to the target oxidation-reduction reaction, the competitive hydrolysis reaction must be considered during the electrode reaction process, as it could interfere with the acquisition of the target substance signal.

Generally, the wider potential window the electrode possessed, the more types of substances could be analyzed, especially those with higher redox potentials. **Figure 2a** showed the (CV) curves of a-C and N doped a-C electrodes, measured in 3.5 wt% NaCl solution (in deionized water) at a scan rate of 100 mV/s. As was shown in Figure 2b, the pure a-C electrode exhibited the widest potential window, close to 4.5 V. The potential window was 3.9 V, 3.9 V, 3.7 V, 3.5 V and 3.1 V for N-2.1 at. %, N-4.0 at. %, N-6.9 at. %, N-12.9 at. % and N-13.1 at. % electrode, respectively. Although, the potential window gradually diminished as the doping N element increased, it retained a relatively wide potential. This might be attributed to the increased surface activity and hydrophilicity caused by N doping and the increase of sp^2-C, which enhanced the adsorption of water molecules on the electrode surface and promoted electron transport.

Subsequently, the electrochemical behavior of a-C and N doped a-C electrodes was evaluated by Fe(CN)$_6{}^{3-}$/Fe(CN)$_6{}^{4-}$ redox system, a simple single electron redox couple. Figure 2c demonstrated the CV measurements in 10 mM K$_3$[Fe(CN)$_6$] (in 1 M HCl solution) with the scan rate of 100 mV/s. The potential separations (ΔE$_p$) between anodic peak and cathodic peak, as well as the ratio of anodic and cathodic peak currents (I_p^{ox}/I_p^{red}) were presented in **Table 1**. Compared with the a-C electrode, even a small amount of nitrogen doping significantly reduced ΔEp in the N-2.1 at.% sample. And ΔEp first increased and then decreased, with the minimum value, 250 mV, appeared in N-12.9 at.% sample. In addition, in N-12.9 at.% sample, the anodic and cathodic peak current density also reached the maximum and the / was closer to 1. These results indicated that the N-12.9 at.% electrode had a more reversible electrode reaction, a higher electrochemical activity and superior catalytic ability for the redox of Fe(CN)$_6{}^{3-}$/Fe(CN)$_6{}^{4-}$ redox couple.

Representatively, the EIS Nyquist plots were performed to analyze the electron transfer capacity of three typical films a-C, N-12.9 at.%, and N-13.1 at.% with a frequency range of

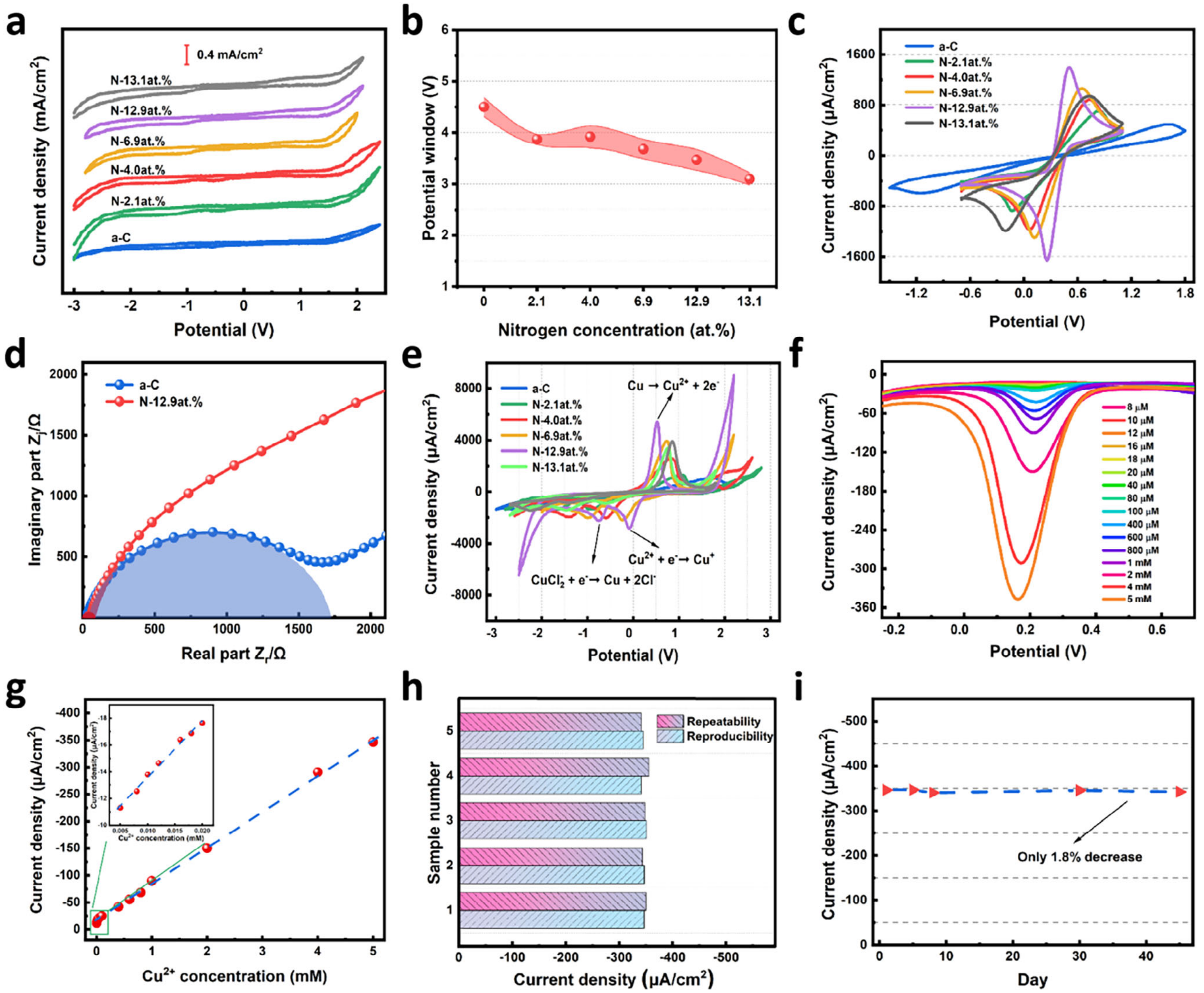

Figure 2. a) CV curves and b) potential windows of a-C and N doped a-C electrodes in 3.5 wt % NaCl solution (in deionized water) with the scan rate of 100 mV s^{-1}; c) CV curves, and d) EIS Nyquist plots with a frequency range of 10^5–0.1 Hz of a-C and N doped a-C electrode in the solution with 10 mM $K_3[Fe(CN)_6]$ (1 M HCl as the solvent); e) CV curves of a-C and N doped a-C electrodes; f) DPV curves and g) the relationship between current peak density and Cu^{2+} concentration with Cu^{2+} concentration from 8×10^{-3} to 5 mM; h) Peak current density for repeatability and reproducibility tests; i) Stability test conducted by DPV measurement, in $CuCl_2$ solution (3.5 wt % NaCl as the solvent), with the scan rate of 100 mV s^{-1}.

Table 1. The ΔE_p and I_p^{ox}/I_p^{red} of electrodes in 10 mM ($K_3[Fe(CN)_6]$) (in 1 M HCl solution).

Electrode number	ΔE_p [V]	I_p^{ox}/I_p^{red}
a-C	2.78	0.836
N-2.1 at.%	0.94	0.800
N-4.0 at.%	0.67	0.757
N-6.9 at.%	0.54	0.817
N-12.9 at.%	0.25	0.844
N-13.1 at.%	0.94	0.790

10^5–0.1 Hz. As shown in Figure 2d, the EIS plots consisted of a semicircle in the high-frequency region and a linear region in the low-frequency region, corresponding to the charge transfer resistance (R_{ct}) and the diffusion process, respectively.[61] Obviously, the N-12.9 at.% had a lower R_{ct} than a-C and N-13.1 at.%, as indicated by the smaller semicircle diameter, which suggested the lower resistivity and faster electron transfer.[62] This finding was consistent with the results of CV measurement shown in Figure 2c.

Figure 2e shows the electrochemical behavior of Cu^{2+} on the electrode surface. The CV measurements of five electrodes were conducted in $CuCl_2$ solution (3.5 wt.% NaCl as the solvent) with a scan rate of 100 mV s^{-1}. Two separate reduction peaks and one oxidation peak were observed in the five CV curves. This was primarily attributable to the high concentration of Cl$^-$, which tended to react with active Cu$^+$ ions, forming a significant amount of $CuCl_2^-$. In 3.5 wt.% NaCl solution, nearly all the Cu$^+$ converted to

Table 2. Repeatability and reproducibility test conducted by DPV measurement in the solution containing 5 mM $CuCl_2$ and 3.5 wt.% NaCl.

Repeatability of a-C:N electrode

Electrode number	1	2	3	4	5
Current density (μA cm^{-2})	−350.20	−344.11	−348.21	−355.42	−341.86
Average current density (μA cm^{-2})			347.96		
RSD			1.37%		

Reproducibility of a-C:N electrode

Electrode number	1	2	3	4	5
Current density (μA cm^{-2})	−346.78	−347.31	−350.89	−341.62	−345.15
Average current density (μA cm^{-2})			346.35		
RSD			0.87%		

$CuCl_2^-$, with the redox electrochemical steps of Cu^{2+} interpreted as follows:

$$Cu^{2+} + e^- \rightarrow Cu^+ \tag{2}$$

$$Cu^+ + 2Cl^- \rightarrow CuCl_2^- \tag{3}$$

$$CuCl_2^- + e^- \rightarrow Cu + 2Cl^- \tag{4}$$

$$Cu \rightarrow Cu^{2+} + 2e^- \tag{5}$$

From the CV curves, the original a-C electrode had a wider potential separation and lower peak current. However, with even a modest amount of N doping, the peak potential separation became narrower, and the peak current density significantly increased. When the nitrogen concentration reached 13.1 at.%, the peak separation further increased, and the peak current signal got weaker than N-12.9 at.%. Therefore, the N-12.9 at.% electrode showed the best performance for Cu^{2+} detection.

2.3. Detection of Cu^{2+}

The Cu^{2+} detection performance of the N-12.9 at.% electrode was investigated by DPV method, due to its higher sensitivity and lower non-vector background current interference. Figure 2f shows the DPV curves of the first cathodic peak in the $CuCl_2$ solution (3.5 wt.% NaCl as the solvent) with Cu^{2+} concentration ranging from 8 to 5 mM. The reduction peak for Cu^{2+}/Cu^+ appeared at 0.19 V, and the peak current density obviously increased as the Cu^{2+} concentration increased. Figure 2g depicts the trend of peak current density and Cu^{2+} concentration, which could be described as a two-stage linear relationship. At the first stage, ranging from 8×10^{-3} mM to 2×10^{-2} mμ, the equation was represented as ipa (μA mM^{-1}) = −9.33–426.10 × C (mM) (R^2 = 0.992). At the second stage, which ranged from 2×10^{-2} mμ to 5 mM, the equation could be depicted as ipa (μA mM^{-1}) = −16.76–67.05 × C (mM) ($R^2 = 0.999$). Therefore, the linear range extended from $8 \times 10^{-3}$to 5 mM. The detection limit was estimated to be 8×10^{-3} mM, which covered the low limit of Cu^{2+} concentration (0.1 mM) in copper alloy crevice corrosion micro-environment.[2]

Further, the repeatability, reproducibility, and stability of the electrode were confirmed. The repeatability test of Cu^{2+} detection was carried out by collecting DPV current signal on the same electrode in five independent solutions containing 5 mM $CuCl_2$ (in 3.5 wt.% NaCl). The DPV curves were shown in Figure S5 (Supporting Information), and peak current density was shown in Figure 2h where only a slight change was observed, with a relative standard deviation (RSD) of 1.37% (shown in **Table 2**), demonstrating the excellent repeatability of Cu^{2+} detection. The reproducibility was evaluated by conducting the DPV measurement on five different electrodes in 5 mM $CuCl_2$ (in 3.5 wt.% NaCl) solution. The DPV measurements and peak current density were shown in Figure S6 (Supporting Information) and Figure 2h, with an RSD of 0.87% (Table 2), implying reliable reproducibility. To assess stability, the electrode was placed in 3.5 wt.% NaCl solution at ambient temperature for a period of time. The peak current signal in Figure 2i was obtained through DPV test in 5 mM $CuCl_2$ (in 3.5 wt.% NaCl) solution. After 45 days of storage, the peak signal showed only 1.8% loss compared with the original state, which might be due to factors such as corrosion, surface fouling or structural degradation of the N-doped a-C film. The phenomenon indicated the well-standing stability of N-doped a-C electrode in the simulated seawater environment with high salt. The detection performance of the N-doped electrode was compared with that of the recently reported copper ion sensor, as shown in Table S1 (Supporting Information).

3. Theoretical Calculations

To study the influence of N element on the a-C structure, the formation energy of the N-doped a-C structure ($\Delta E^f_{a-C:N}$) was calculated using the following formula:[63]

$$\Delta E^f_{a-C:N} = \left(E^{total}_{a-C:N} + E^{atom}_{C}\right) - \left(E^{total}_{a-C} + E^{atom}_{N}\right) \tag{6}$$

where E^{total}_{a-C} and $E^{total}_{a-C:N}$ represent the total energies of the a-C structure and the N-doped a-C structure respectively, E^{atom}_{C} and E^{atom}_{N} represent the energies of a single C atom and N atom, respectively. The formation energy ($\Delta E^f_{a-C:N}$) can largely reflect the stability status of the N-doped a-C structure. Specifically, the smaller the value is, the more stable the N-doped a-C structure tends to be. Based on the sp^2 ratio of a-C measured in the experiment and limited by the first principles calculation system, two types of N-doped a-C structures with the sp^2 hybridized C ratios of 53.13% and 78.13%. The specific situations are shown in Figure S9 (Supporting Information). Subsequently, for these two different structures, we calculated their respective formation energies in detail, and the relevant data are presented in Table S2 (Supporting Information). Through calculation and analysis, it was found that the formation energy corresponding to the N-doped a-C structure with the sp^2 hybridized C ratio of 78.13% is relatively greater. This result fully indicates that in the a-C structure, when the sp^2 hybridized C ratio is at a higher level (such as 78.13% in this research), it is easier to dope the a-C structure with N elements, and the formed doped structure also has better stability.

For the atomic adsorption model, the adsorption energy can effectively characterize the adsorption effect of atoms on the surface. To describe the adsorption strength of Cu ions by different models, a more accurate single-point energy self-consistent calculation was carried out on the basis of the relaxation structures. The formula for calculating the adsorption energy is as follows: [64]

$$E_{ads} = E_{sub/ad} - E_{sub} - E_{ad} \tag{7}$$

where $E_{sub/ad}$ is the total energy of the adsorption model; E_{sub} is the energy of the substrate, and E_{ad} is the energy of the adsorption atom/ion. When the adsorption energy takes on a negative value, it means that the adsorption process can proceed spontaneously, and the larger its absolute value is, the stronger the adsorption ability will be. By calculating the adsorption energy (E_{ads}) of two sp^2 hybrid C ratios a-C structures, and their corresponding doped N structures at different interfacial distances, the optimal adsorption position of Cu ions on the a-C structure surface was determined, and the structure was sufficiently relaxed (Figure S10, Supporting Information). The calculation results indicate that, on the surface of the undoped a-C structure, the displacement of Cu ions before and after relaxation is rather limited, thereby leading to a minor variation in the adsorption energy of Cu ions. In contrast, on the surface of the N-doped a-C structure, Cu ions exhibit a stronger propensity to be adsorbed onto the surface of C atoms instead of N atoms after relaxation, which consequently gives rise to a more significant change in the adsorption energy of Cu ions. Overall, the increase in the sp^2 hybrid C ratios is helpful for enhancing the adsorption energy of a-C toward Cu ions, and the N-doping is also beneficial for improving this adsorption energy. Under such circumstances, the N-doped a-C with sp^2 hybridized C ratio of 78.13% exhibits the best adsorption effect, which is consistent with the experimental results.

The charge density difference (CDD) is a widely used tool in materials science and quantum chemistry. It is used to study the changes in charge distribution of a system in different states (such as before and after atomic bonding). It is obtained by subtracting the superposition of the charge densities of isolated atoms from the total charge density of the system. It allows one to visually observe the redistribution of electrons when atoms form chemical bonds or undergo other interactions. During the electrochemical sensing process, charge transfer occurs between a-C and Cu ions. By calculating the CCD, it is possible to determine which regions at the interface between a-C and Cu ions have experienced charge accumulation or loss, thus understanding the direction and extent of charge transfer. The calculation formula for the CCD of the adsorption model is as follows:[65]

$$\Delta\rho = \rho_{sud/ad} - \rho_{sud} - \rho_{ad} \tag{8}$$

where $\rho_{sud/ad}$ is the total CCD of the adsorption model; ρ_{sud} is the CCD of the substrate, and ρ_{ad} is the CCD of the adsorption atom/ion. The CCD of the Cu ion adsorption models for two types of sp^2 hybridized C ratio a-C structures and their corresponding doped N structures were calculated, as shown in **Figure 3**. The brownish-red areas and dark green areas in the figure represent the charge accumulation and charge loss after the adsorption of Cu ions, respectively. It can be seen that there is an obvious charge loss around the Cu ions. To further analyze the impact of the Cu ion adsorption process on the charge states of C atoms and N atoms in a-C, select the plane determined by these three atoms to draw a 2D CCD diagram. In the diagram, the red areas, blue areas, and green areas represent the charge accumulation, charge loss, and unchanged charge distribution after the adsorption of Cu ions, respectively. It can be seen that there is a charge loss around Cu ion and C atom. The lost charges gather and superimpose between Cu ion and C atom, thus forming bonding orbitals. The probability of electrons appearing in the region between the two nuclei is increased, and finally, a covalent bond is formed. Similarly, in Figure 3c, a covalent bond is also formed between Cu ion and N atom. However, due to the relatively low probability of electron accumulation, the strength of the Cu—N bond is weaker than that of the Cu—C bond, which explains the phenomenon that Cu ions are more likely to be adsorbed on the surface of C atoms rather than that of N atoms after relaxation. In Figure 3d, the adsorption of Cu ions will cause a charge loss between the C atom and N atom, which means that Cu ions will weaken the binding strength of the C—N bond.

To further analyze the bonding characteristics of Cu ions on the a-C surface, the density of states (DOS) of Cu ions, N atoms, C atoms, and a-C structures was calculated, as shown in Figure 3. It was found that within the energy range of -8 to 0 eV, there is a resonance between the d orbital of Cu ions and the p orbital of C atoms (or N atoms); and within the energy range of 0 to 6 eV, the p orbital of Cu ions and the p orbital of C atoms (or N atoms) also have a resonance. The above phenomenon indicates that the DOS of Cu ions and that of C atoms (or N atoms) have a relatively wide overlapping region. It can be inferred that when Cu ions are adsorbed on the a-C surface, relatively strong covalent bonds will be formed with C atoms (or N atoms).

During the electrochemical sensing process, electron transfer occurs between the electrode materials and the substances to be detected. The changing trend of the density of states near the Fermi level (E_f) reflects the ease or difficulty of electron transitions between different energy levels. If the DOS curve near the Fermi level (E_f) is relatively smooth, it indicates that electron transitions between energy levels in this region are relatively easy, and the electrical properties of the substance are closer to those of metals. If the curve fluctuates greatly or there is an energy gap, electrons need to overcome certain energy barriers during transitions, and the electrical properties of the substance are closer to those of insulators or semiconductors. Through the analysis of the DOS of four a-C structures, it was found that the values at the Fermi level (E_f) were all non-zero. This phenomenon fully

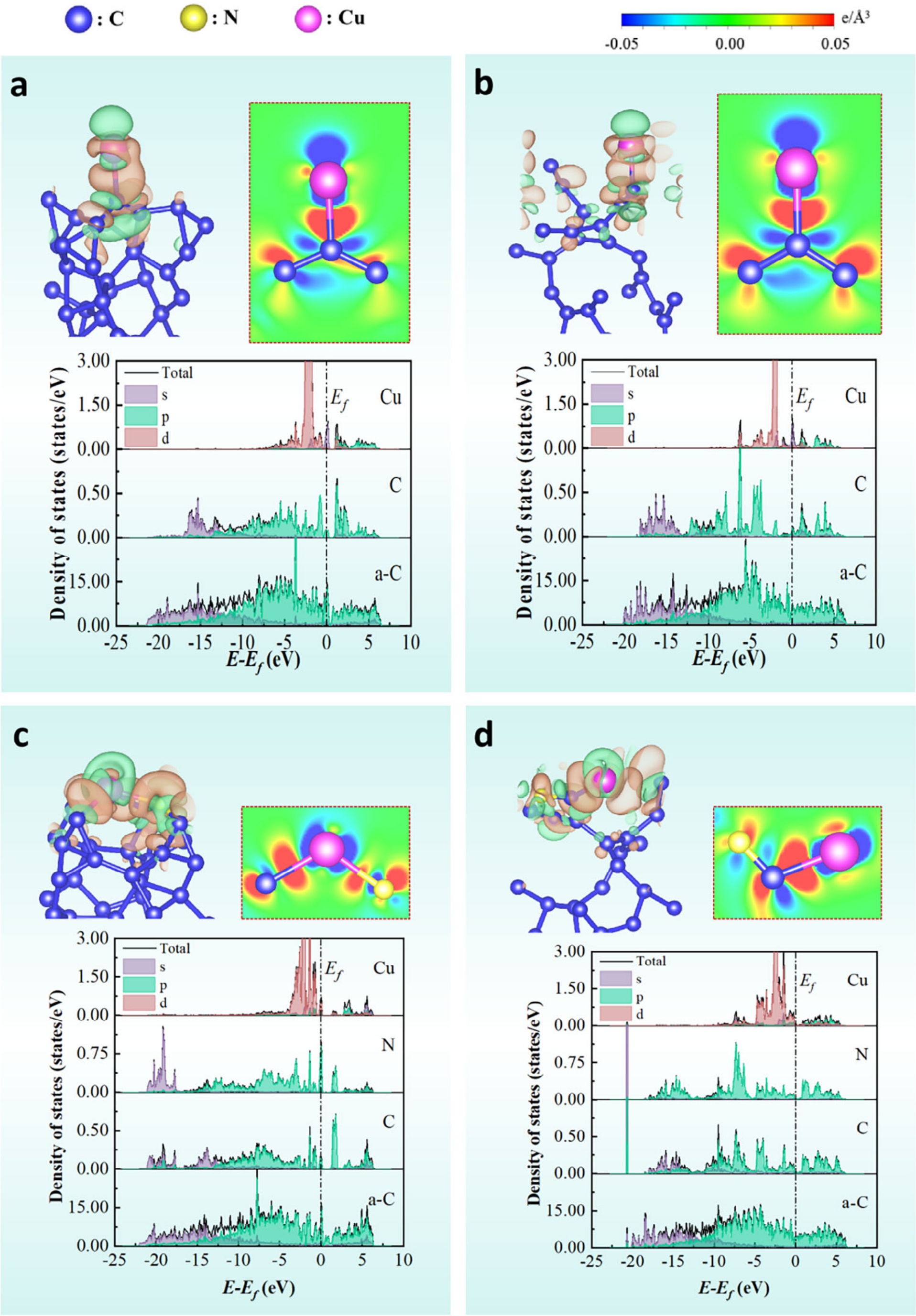

Figure 3. The charge density difference of Cu ion adsorption on a-C surface. a) Undoped a-C (sp^2: 53.13%); b) Undoped a-C (sp^2: 78.13%); c) N-doped a-C (sp^2: 53.13%); d) N-doped a-C (sp^2: 78.13%).

confirms the existence of free electrons inside. Moreover, as the sp^2 hybridized C ratio increases and N-doping is involved, both will prompt the DOS curve near the Fermi level (E_f) to become smoother. This enables the N-doped a-C with an sp^2 hybridized C ratio of 78.13% to exhibit the best electron transport effect, which is highly consistent with the results obtained from experiments.

According to the microstructure evolution, electrochemical performance changes, and theoretical calculations of the interior and surface of the film before and after nitrogen doping, **Figure 4** shows the electrochemical behavior of the N-doped a-C film. As described above, after nitrogen doping, the film showed better reversibility, stronger electrochemical signal, and enhanced electron transfer. This was mainly due to the improved conductivity of a-C film and enhanced electrochemical activity at the film surface. On the one hand, XPS and Raman results confirmed that an appropriate amount of N doping not only

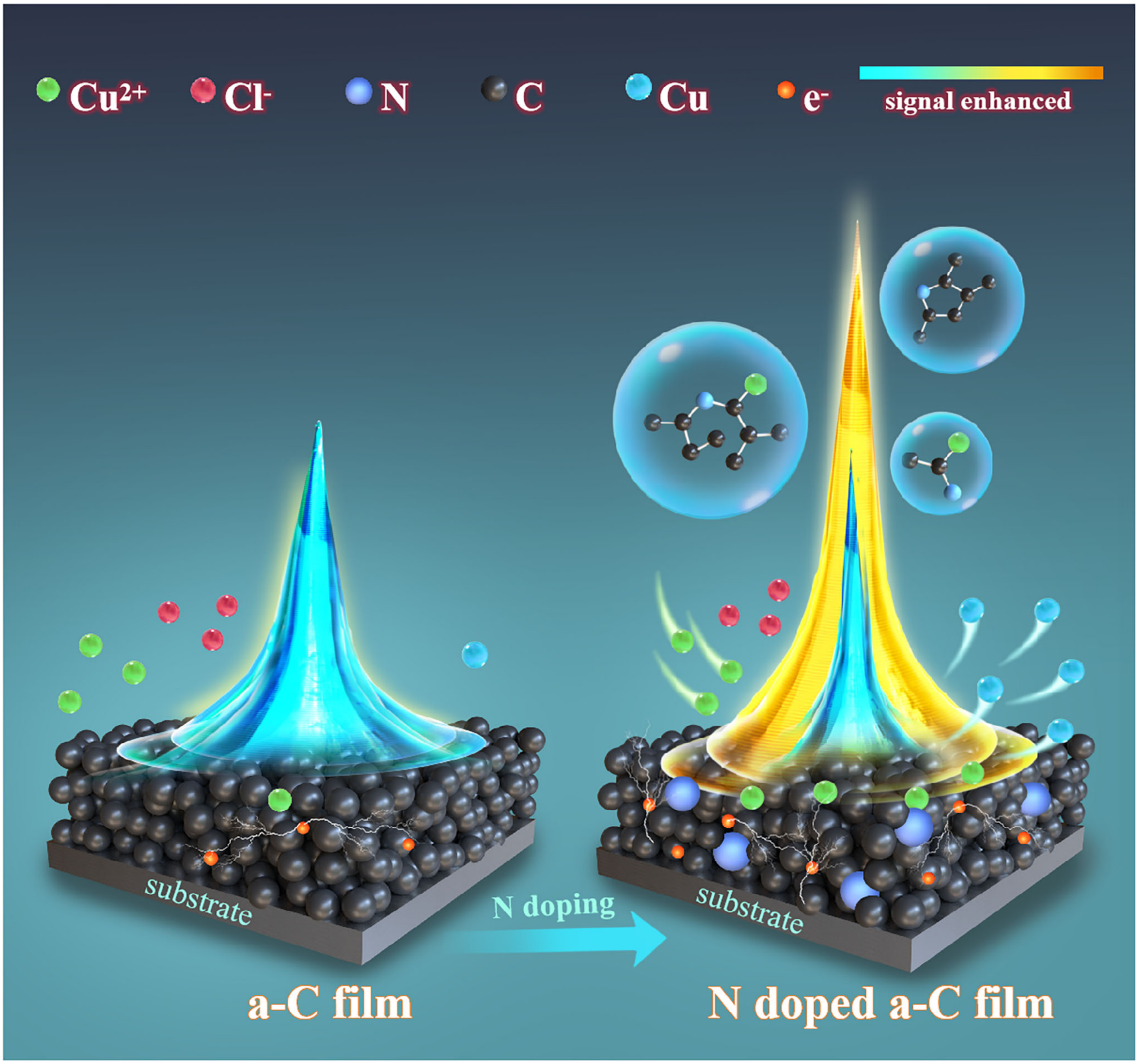

Figure 4. Schematic diagram of electron transfer and electrochemical behavior of a-C and N doped a-C film.

promoted the sp^2-C fraction but also enhanced the formation of larger size sp^2 graphite grains, thereby enhancing the conductivity of the film.[66] On the other hand, after nitrogen doping, more active nitrogen-containing groups were formed on N-doped a-C film surface, benefiting active sites formation, thus enhancing the electrochemical reaction.[67] Therefore, an appropriate amount of N doping enhanced graphitization and improved surface activity were the main reasons for the improvement of electrochemical performance.

4. Conclusion

In summary, the nitrogen doped amorphous carbon films were successfully prepared by linear ion beam technique, with nitrogen concentrations ranging from 0 to 13.1 at.% could be achieved by regulating the ratio of N_2:C_2H_2 flow rate from 0:100 to 85:15. It was noteworthy that due to the high ionization of linear ion beam, the N doped a-C films showed improved conductivity together with the anti-corrosion of a-C matrix. The introduced nitrogen formed chemical bonds with carbon atoms such as C═O. Most importantly, the moderate N doping could promote the formation of sp^2-C cluster sites. In addition, the N doping film maintained the amorphous nanostructure, and the film surface became smoother with the addition of N elements. The N-12.9 at.% electrode showed better reversibility, stronger electrochemical activity, and faster electron transfer. Theoretical calculations explained this result in detail. Moderate N doping promotes the formation of sp^2-C and improves the conductivity. At the same time, the N—C, N═C and other active bonds formed after nitrogen doping enhanced the adsorption of copper ions on the electrode surface, thus improving the detection performance of the sensor. By DPV method, the linear range for Cu^{2+} detection was 8×10^{-3} to 5 mM and the detection limit was estimated to be 8×10^{-3} mM in 3.5 wt.% NaCl solution, which covered the low limit of Cu^{2+} concentration (0.1 mM) in copper alloy crevice corrosion microenvironment. In conclusion, the good Cu^{2+} detection performance together with the well-standing repeatability, reproducibility, and stability manifested the great potential of nitrogen-doped a-C films used for marine corrosion detection.

5. Experimental Section

Preparation of N-Doped a-C Film: N-doped a-C films were deposited on highly conductive B-doped Si (110) substrate with the conductivity at 0.001–0.005 Ω.cm by a hybrid ion beam deposition system with an ALIS. Prior to deposition, the Si substrates were cleaned by ultrasonic in acetone for 10 min and then dried at room temperature. After the chamber was evacuated $<2.0 \times 10^{-5}$ Torr, the Si substrates located on the jig holder were precleaned by ALIS with Ar ions at a negative pulsed bias voltage of −100 V and argon flow rate of 40 sccm for 10 min to remove the contamination on the surface. During deposition, C_2H_2 and N_2 were introduced to the ALIS as a mixed gas source. The work chamber pressure was kept at 5.6×10^{-3} Torr and the substrate bias voltage was set at −550 V. By regulating the gas flow rate of N_2 and C_2H_2 (N_2:C_2H_2 = 0:100, 20:80, 40:60, 60:40, 80:20, 85:15), a series of N-doped a-C films with different nitrogen concentrations were prepared. By adjusting deposition time, the thickness of film was controlled between 200 to 300 nm.

Electrochemical Tests: The N-doped a-C film working electrodes for electrochemical tests were fabricated as follows. First, the Si substrate with N-doped a-C film was tailored into 1.2 × 1.2 cm square. Then the Cu wire was connected with the film by silver conductive glue. After that, the edges and joints were sealed with epoxy resin and silicone resin, and the electrode was done with 1 × 1 cm testing window. The reagent sources of NaCl and HCl were purchased from Sinopharm Chemical Reagent Co. Ltd., China. $CuCl_2$ and $K_3[Fe(CN)_6]$ were obtained from RHAWN. The electrochemical experiments were carried out in a three-electrode electrochemical cell system with Ag/AgCl (KCl saturated), platinum plate, N-doped a-C film as the reference electrode, counter electrode, and working electrode, respectively. The electrochemical tests were performed at CHI electrochemical instrument (CHI1220c, CH Instruments, China). All the experiments were carried out at room temperature (25 °C).

Materials Characterization: The chemical composition of N-doped amorphous carbon films was analyzed by X-ray photoelectron spectroscopy (XPS, Axis Supra, Kratos, Shimadzu, Japan) utilizing a monochromatic Al Kα X-ray source. To calibrate the binding energy, the C 1s peak was located at 284.5 eV as reference. The atomic bond changes of these films were characterized by Raman spectra (InVia Reflex, Renishaw, UK) with a 532 nm exciting wavelength. The N-doped a-C film specimens for transmission electron microscope were prepared by focused ion beam (FIB, Helios-G4-CX, Thermo Scientific, USA). The high-resolution transmission electron microscopy (HRTEM) images of cross-section and the selected area electron diffraction (SAED) were conducted by transmission electron microscope (TEM, Tecnai F20, FEI, USA). The changes of sp^2 and sp^3 bonds were also investigated by electron energy loss spectroscopy (EELS) using the scanning transmission electron microscope (STEM, Tecnai F20, FEI, USA). The surface morphology and roughness of the films were investigated by scanning probe microscopy (SPM, Dimension 3100, Veeco, USA). The contact angle measuring instrument (OCA20, DataPhysics, Germany) was employed to determine the wettability of the film surface.

Calculation Method: The a-C structure (Figure S7, Supporting Information) was constructed using the first-principles calculation software VASP (Vienna Ab-initio Simulation Package) with the melt-quenching method.[68–71] According to the required sp^2 ratio, 64 carbon atoms were randomly filled into a simple cubic unit cell with specific lattice constants and periodic boundary conditions. First, under the regulation of the Nose-Hoover thermostat[72,73] and NVT (canonical) ensemble[74] based on the ab initio molecular dynamics (AIMD) method,[75] the system was relaxed for 1 ps at a temperature of 8000 K to completely melt its internal structure. Then, the temperature of the system was rapidly decreased from 8000 K to 1 K within 0.5 ps. Finally, the conjugate gradient algorithm based on the DFT was used to the geometric optimization (GO) of the system.[76–79] The simulation was ended when the Hellman-Feynman force on each atom was <0.01 eV Å^{-1}, and the electronic self-consistent energy was $<10^{-5}$ eV, and the final a-C structure was obtained. The radial distribution function (RDF) curves of a-C films with a sp^2 ratio of 53.13% and 78.13%, respectively, were shown in Figure S8 (Supporting Information).

Supporting Information

Supporting Information is available from the Wiley Online Library or from the author.

Acknowledgements

X.Z. and S.Z. contributed equally to this work. The authors acknowledge the National Science Foundation for Distinguished Young Scholars of China (No. 52025014), the Zhejiang Provincial Natural Science Foundation of China (No. LD24E010003), and the Natural Science Foundation of Ningbo Municipality (No.2023J410).

Conflict of Interest

The authors declare no conflict of interest.

Data Availability Statement

The data that support the findings of this study are available from the corresponding author upon reasonable request.

Keywords

amorphous carbon film, copper ion, electrochemical detection, marine corrosion, N doped

Received: June 23, 2025
Published online:

---

[1] A. Cranny, N. R. Harris, M. Y. Nie, J. A. Wharton, R. J. K. Wood, K. R. Stokes, *IEEE Sens. J.* **2012**, *12*, 2091.
[2] J. A. Wharton, R. C. Barik, G. Kear, R. J. K. Wood, K. R. Stokes, F. C. Walsh, *Corros. Sci.* **2025**, *47*, 3336.
[3] J. A. Wharton, K. R. Stokes, *Electrochim. Acta.* **2008**, *53*, 2463.
[4] T. Dobson, N. Larrosa, M. Reid, K. Rajamudili, S. Ganguly, H. Coules, *Corros. Sci.* **2024**, *232*, 112004.
[5] J. A. Wharton, K. R. Stokes, *Electrochem. Commun.* **2007**, *9*, 1035.
[6] J. Chen, D. Sun, S. Xu, Y. Fu, Y. Yang, J. Ma, *Adv. Mater. Interfaces* **2022**, *9*, 2200491.
[7] I. Kaur, M. Sharma, S. Kaur, A. Kaur, *Sens. Actuator B-Chem.* **2020**, *312*, 127935.
[8] D. Maddipatla, T. S. Saeed, B. B. Narakathu, S. O. Obare, M. Z. Atashbar, *IEEE Sens. J.* **2020**, *20*, 12582.

[9] Y. Li, Z. Shi, C. Zhang, X. Wu, L. Liu, C. Guo, C. M. Li, *J. Colloid Interface Sci.* **2021**, *603*, 131.
[10] F. Chen, M. Zhao, B. Zhang, M. Zhao, Y. Ma, *Sensors* **2024**, *24*, 3809.
[11] M. Zhou, L. Han, D. M. Deng, Z. Zhang, H. B. He, L. Zhang, L. Q. Luo, *Sens. Actuator B-Chem.* **2019**, *91*, 164.
[12] S. Nakabayashi, D. A. Tryk, A. Fujishima, N. Ohta, *Chem. Phys. Lett.* **1999**, *300*, 409.
[13] P. Ashcheulov, O. Hák, S. Sedláková, A. Taylor, S. Baluchová, K. Schwarzová-Pecková, M. Davydova, J. Kopeček, L. Klimša, M. Vondráček, J. Honolka, V. Mortet, *Adv. Mater. Interfaces* **2022**, *9*, 2200375.
[14] K. E. Toghill, L. Xiao, M. A. Phillips, R. G. Compton, *Sens. Actuator B-Chem.* **2010**, *147*, 642.
[15] L. J. Simcox, R. P. A. Pereira, E. M. H. Wellington, J. V. Macpherson, *ACS Appl. Mater. Interfaces* **2019**, *11*, 25024.
[16] J. Pei, X. Yu, Z. Zhang, J. Zhang, S. Wei, R. Boukherroub, *Appl. Surf. Sci.* **2020**, *527*, 146761.
[17] M. Nie, S. Neodo, J. A. Wharton, A. Cranny, N. R. Harris, R. J. K. Wood, K. R. Stokes, *Electrochim. Acta.* **2016**, *202*, 345.
[18] Z. Liu, A. F. Sartori, J. G. Buijnsters, *Electrochem. Commun.* **2021**, *130*, 107096.
[19] P. Joshi, P. Riley, S. Gupta, R. Narayan, J. Narayan, *Nanotechnology* **2021**, *32*, 432001.
[20] Y. Tanaka, M. Furuta, K. Kuriyama, R. Kuwabara, Y. Katsuki, T. Kondo, A. Fujishima, K. Honda, *Electrochim. Acta.* **2011**, *56*, 1172.
[21] A. Benchikh, C. Debiemme-Chouvy, H. Cachet, A. Pailleret, B. Saidani, L. Beaunier, M. H. Berger, C. Deslouis, *Electrochim. Acta.* **2012**, *75*, 131.
[22] C. Y. Jin, A. P. Zeng, S. J. Cho, J. H. Boo, *J. Korean Phys. Soc.* **2012**, *60*, 912.
[23] N. Liu, H. K. Zhu, Q. P. Wei, H. Y. Long, Z. J. Deng, Z. M. Yu, Y. N. Xie, J. Wang, L. Ma, K. C. Zhou, *J. Electrochem. Soc.* **2017**, *164*, H1091.
[24] B. Rothammer, M. Schwendner, M. Bartz, S. Wartzack, T. Böhm, S. Krauß, B. Merle, S. Schroeder, M. Uhler, J. P. Kretzer, V. Weihnacht, M. Marian, *Adv. Mater. Interfaces* **2023**, *10*, 2202370.
[25] Z. A. Boeva, A. Catena, L. Hofler, S. Wehner, C. B. Fischer, T. Lindfors, *Carbon* **2017**, *120*, 157.
[26] L. Li, L. L. Liu, X. W. Li, P. Guo, P. L. Ke, A. Y. Wang, *ACS Appl. Mater. Interfaces* **2018**, *10*, 13187.
[27] J. Wei, H. Li, L. Liu, P. Guo, P. Ke, A. Wang, *Surf. Coat. Technol.* **2019**, *374*, 317.
[28] H. Li, P. Guo, D. Zhang, R. D. Chen, X. Zuo, P. L. Ke, H. Saito, A. Y. Wang, *Appl. Surf. Sci.* **2020**, *503*, 144310.
[29] J. Wei, P. Guo, L. L. Liu, H. C. Li, H. Li, S. Y. Wang, P. L. Ke, H. Saito, A. Y. Wang, *Electrochim. Acta.* **2020**, *346*, 136282.
[30] J. Wei, P. Guo, L. L. Liu, H. C. Li, H. Li, S. Y. Wang, P. L. Ke, A. Y. Wang, *Appl. Surf. Sci.* **2020**, *516*, 146115.
[31] A. Liu, H. Wu, X. Qiu, W. Tang, *J. Nanosci. Nanotechnol.* **2011**, *11*, 11064.
[32] M. Liu, X. Zhu, Y. Song, G. Huang, J. Wei, X. Song, Q. Xiao, T. Zhao, W. Jiang, X. Li, W. Luo, *Adv. Funct. Mater.* **2023**, *33*, 2213395.
[33] C. Wang, Z. Zhao, W. Cao, Y. Peng, M. Song, Y. Wu, *Adv. Funct. Mater.* **2025**, 2502618.
[34] Y. S. Zou, L. L. He, Y. C. Zhang, X. Q. Shi, Z. X. Li, Y. L. Zhou, C. J. Tu, L. Gu, H. B. Zeng, *J. Appl. Electrochem.* **2013**, *43*, 911.
[35] Q. K. Zhou, P. L. Ke, X. W. Li, Y. S. Zou, A. Y. Wang, *Appl. Surf. Sci.* **2015**, *329*, 281.
[36] A. K. Thakur, K. Kurtyka, M. Majumder, X. Yang, H. Q. Ta, A. Bachmatiuk, L. Liu, B. Trzebicka, M. H. Rummeli, *Adv. Mater. Interfaces* **2022**, *9*, 2101964.
[37] X. M. He, K. C. Walter, M. Nastasi, *J. Phys.: Condens. Matter.* **2000**, *12*, L183.
[38] X. Mou, J. Ma, S. Zheng, X. Chen, F. Krumeich, R. Hauert, R. Lin, Z.-S. Wu, Y. Ding, *Adv. Funct. Mater.* **2021**, *31*, 2006076.
[39] A. Liu, J. Han, J. Zhu, S. Meng, X. He, *Mater. Sci. Eng. C.* **2008**, *28*, 1408.
[40] M. Nilkar, F. E. Ghodsi, S. Jafari, D. Thiry, R. Snyders, *J. Alloys Compd.* **2021**, *853*, 157298.
[41] T. F. Zhang, Q. X. Xia, Z. X. Wan, J. M. Yun, Q. M. Wang, K. H. Kim, *Chem. Eng. J.* **2019**, *360*, 1310.
[42] H. Hu, J. H. Xin, H. Hu, X. Wang, Y. Kong, *Appl. Catal. A-Gen.* **2015**, *492*, 1.
[43] A. Shakil, A. Amiri, H. Tang, A. A. Polycarpou, *Appl. Surf. Sci.* **2021**, *535*, 147662.
[44] S. Wang, C. Han, J. Wang, J. Deng, M. Zhu, J. Yao, H. Li, Y. Wang, *Chem. Mater.* **2014**, *26*, 6872.
[45] O. L. Li, K. Prabakar, A. Kaneko, H. Park, T. Ishizaki, *Catal. Today* **2019**, *337*, 102.
[46] B. Li, X. Sun, D. Su, *Phys. Chem. Chem. Phys.* **2015**, *17*, 6691.
[47] J. Zhou, N. Lin, W. Cai, C. Guo, K. Zhang, J. Zhou, Y. Zhu, Y. Qian, *Electrochim. Acta* **2016**, *218*, 243.
[48] H. L. Bai, E. Y. Jiang, *Thin Solid Films* **1999**, *353*, 157.
[49] A. C. Ferrari, *Diamond Relat. Mater.* **2002**, *11*, 1053.
[50] A. R. Merchant, D. R. McKenzie, D. G. McCulloch, *Phys. Rev. B.* **2001**, *65*, 0242.
[51] B. Zheng, W. T. Zheng, K. Zhang, Q. B. Wen, J. Q. Zhu, S. H. Meng, X. D. He, J. C. Han, *Carbon* **2006**, *44*, 962.
[52] K. Zhou, P. Ke, Z. Jiang, A. Wang, Y. Zou, *Chin. J. Mater. Res.* **2014**, *28*, 161.
[53] M. Liang, Y. Ren, J. Cui, X. Zhang, S. Xing, J. Lei, M. He, H. Xie, L. Deng, F. Yu, J. Ma, *Nat. Commun.* **2024**, *15*, 6437.
[54] M. H. Ahmed, J. A. Byrne, *Appl. Surf. Sci.* **2012**, *258*, 5166.
[55] J. J. Cuomo, J. P. Doyle, J. Bruley, J. C. Liu, *Appl. Phys. Lett.* **1991**, *58*, 466.
[56] J. Xie, K. Komvopoulos, *J. Appl. Phys.* **2016**, *119*, 91.
[57] S. Sainio, D. Nordlund, M. A. Caro, R. Gandhiraman, J. Koehne, N. Wester, J. Koskinen, M. Meyyappan, T. Laurila, *J. of Phys. Chem. C.* **2016**, *120*, 8298.
[58] T. Palomäki, N. Wester, M. A. Caro, S. Sainio, V. Protopopova, J. Koskinen, T. Laurila, *Electrochim. Acta* **2017**, *225*, 1.
[59] S. Srinivasan, Y. Tang, Y. S. Li, Q. Yang, A. Hirose, *Appl. Surf. Sci.* **2012**, *258*, 8094.
[60] Wenzel, N. R., *J. Phys. Colloid Chem.* **1949**, *53*, 1466.
[61] Y. S. Hei, X. Q. Li, X. Zhou, J. J. Liu, M. Hassan, S. Y. Zhang, Y. Yang, X. J. Bo, H. L. Wang, M. Zhou, *Anal. Chim. Acta.* **2018**, *1029*, 15.
[62] L. Dong, L. Fan, Y. G. Ding, *J. Electrochem. Soc.* **2019**, *166*, B1585.
[63] L. Rao, H. Liu, W. Shao, H. Liu, X. Xing, Y. Zhou, Z. Shi, Q. Yang, *J. Alloys Compd.* **2021**, *868*, 159151.
[64] W. Yang, Z. Gao, X. Liu, X. Ding, W. Yan, *Chem. Eng. J.* **2019**, *361*,304.
[65] R. Topolnicki, R. Kucharczyk, *Appl. Surf. Sci* **2014**, *304*, 115.
[66] X. Li, K. Hou, D. Qiu, P. Yi, X. Lai, *Carbon* **2020**, *167*, 219.
[67] L. X. Liu, E. Liu, *Surf. Coat. Technol.* **2005**, *198*, 189.
[68] G. Kresse, J. Furthmüller, *Phys. Rev. B.* **1996**, *54*, 11169.
[69] G. Kresse, J. Furthmüller, *Comput. Mater. Sci.* **1996**, *6*, 15.
[70] M. M. M. Bilek, D. R. McKenzie, D. G. McCulloch, C. M. Goringe, *Phys. Rev. B.* **2000**, *62*, 3071.
[71] X. Li, P. Ke, A. Wang, *Thin Solid Films* **2015**, *584*, 204.
[72] S. Nosé, *J. Chem. Phys.* **1984**, *81*, 511.
[73] W. G. Hoover, *Phys. Rev. A* **1985**, *31*, 1695.
[74] S. Nosé, *Mol. Phys.* **2002**, *100*, 191.
[75] M. E. Tuckerman, *J. Phys.: Condens. Matter.* **2022**, *14*, R1297.
[76] E. J. Davison, P. Wong, *Automatica* **1975**, *11*, 297.
[77] E. Runge, E. K. U. Gross, *Phys. Rev. Lett.* **1984**, *52*, 997.
[78] J. D. Patterson, *Ann. Nucl. Energy* **1989**, *16*, 611.
[79] A. D. Becke, *J. Chem. Phys.* **1993**, *98*, 5648.